Electronic Supplementary Material (ESI) for Journal of Materials Chemistry A.
This journal is © The Royal Society of Chemistry 2019

Supporting Information

Ambient Fast, Large-Scale Synthesis of Entropy-Stabilized Metal-Organic Framework Nanosheets for Electrocatalytic Oxygen Evolution

Xinhui Zhao,[a] Zhimin Xue,[b] Wenjun Chen,[a] Xiyue Bai,[a] Ruifen Shi,[a] and Tiancheng Mu,[a]*

[a] Department of Chemistry, Renmin University of China, Beijing 100872, China

[b] Beijing Key Laboratory of Lignocellulosic Chemistry, College of Materials Science and Technology, Beijing Forestry University, Beijing 100083, China

*Corresponding Author:

E-mail: tcmu@ruc.edu.cn

Table of Contents

1. Experimental sections
2. **Figure S1.** Illustration of the difference between a) solvothermal reaction and b) solution phase method.
3. **Figure S2.** Crystal structure of HE-MOF-RT.
4. **Figure S3.** FT-IR spectra of HE-MOF-RT, HE-MOF-ST and 1, 4-BDC.
5. **Figure S4.** SEM images of HE-MOF-RT nanosheets.
6. **Figure S5.** AFM image HE-MOF-RT nanosheets.
7. **Figure S6.** a-c) SEM images and d) TEM image of HE-MOF-ST.
8. **Figure S7.** a) N_2 adsorption-desorption isotherm and b) the corresponding pore size distribution of HE-MOF-RT at 77 K.
9. **Figure S8.** a) N_2 adsorption-desorption isotherm and b) the corresponding pore size distribution of Ni-MOF-RT at 77 K.
10. **Figure S9.** a) N_2 adsorption-desorption isotherm and b) the corresponding pore size distribution of HE-MOF-ST at 77 K.
11. **Figure S10.** EDS spectrum of HE-MOF-RT, and the inserted table summarizes the atomic ratio of elements inside HE-MOF-RT.
12. **Figure S11.** SEM-EDS mapping of HE-MOF-RT.
13. **Figure S12.** EDS spectrum of HE-MOF-RT, and the inserted table summarizes the atomic ratio of elements inside HE-MOF-RT.
14. **Figure S13.** SEM-EDS mapping of HE-MOF-ST.
15. **Figure S14.** XPS spectra of a) survey, b) Mn 2p, c) Fe 2p, d) Co 2p, e) Ni 2p and f) Cu 2p of HE-MOF-RT.
16. **Figure S15.** Scheme for a scale-up synthesis of HE-MOF-RT.
17. **Figure S16.** XRD pattern for HE-MOF-RT prepared in a scale-up synthesis.
18. **Figure S17.** TEM image for HE-MOF-RT prepared in a scale-up synthesis.
19. **Figure S18.** EDS spectrum for HE-MOF-RT prepared in a scale-up synthesis.
20. **Figure S19.** XPS spectra of a) survey, b) Mn 2p, c) Fe 2p, d) Co 2p, e) Ni 2p and f) Cu 2p of HE-MOF-RT prepared in a scale-up synthesis.
21. **Figure S20.** Mass activities of different catalysts at various applied potentials.
22. **Figure S21.** a) LSV curve and b) the corresponding Tafel plots of HE-MOF-RT on carbon cloth electrode.
23. **Figure S22.** a) LSV curve and b) the corresponding Tafel plots of HE-MOF-RT prepared in a scale-up synthesis.
24. **Figure S23.** a) XRD pattern and b) EDS spectrum of NiMn-MOF synthesized by the solution phase method under ambient temperature.
25. **Figure S24.** a) XRD pattern and b) EDS spectrum of NiFe-MOF synthesized by the solution phase method under ambient temperature.
26. **Figure S25.** a) XRD pattern and b) EDS spectrum of NiCo-MOF synthesized by the solution phase method under ambient temperature.
27. **Figure S26.** a) XRD pattern and b) EDS spectrum of NiCu-MOF synthesized by the solution phase method under ambient temperature.
28. **Figure S27.** a) XRD pattern and b) EDS spectrum of NiCoMn-MOF synthesized by the solution phase method under ambient temperature.

29. **Figure S28.** a) XRD pattern and b) EDS spectrum of NiCoFe-MOF synthesized by the solution phase method under ambient temperature.
30. **Figure S29.** a) XRD pattern and b) EDS spectrum of NiCoCu-MOF synthesized by the solution phase method under ambient temperature.
31. **Figure S30.** LSV polarization curves of a) bimetallic MOFs and b) trimetallic MOFs in 1 M KOH with a scan rate of 5 mV s^{-1}.
32. **Figure S31.** Double-layer capacitance measurements for determining electrochemically active surface area for HE-MOF-RT catalyst from voltammetry in 1 M KOH.
33. **Figure S32.** Double-layer capacitance measurements for determining electrochemically active surface area for HE-MOF-ST catalyst from voltammetry in 1 M KOH.
34. **Figure S33.** XRD pattern of HE-MOF-RT after stability test.
35. **Figure S34.** TEM image of HE-MOF-RT after stability test.
36. **Figure S35.** EDS spectrum of HE-MOF-RT after stability test.
37. **Figure S36.** XPS spectra of a) survey, b) Mn 2p, c) Fe 2p, d) Co 2p, e) Ni 2p and f) Cu 2p of HE-MOF-RT after stability test.
38. **Table S1.** Content of five metal species in HE-MOF-RT and HE-MOF-ST.
39. **Table S2.** Atomic ratio of five metal elements in HE-MOF-RT and HE-MOF-ST extracted from XPS spectra.
40. **Table S3.** Comparisons of OER performance for recently reported transition metal-based electrocatalysts in 1.0 M KOH electrolyte.
41. **Table S4.** Atomic ratio of bi- and trimetallic MOFs extracted from XPS spectra.
42. References

Experiment Section

Chemicals

Manganese (II) chloride tetrahydrate ($MnCl_2·4H_2O$, ≥99.0%), iron chloride (III) hexahydrate ($FeCl_3·6H_2O$, ≥99.0%), cobalt chloride (II) tetrahydrate ($CoCl_2·6H_2O$, ≥99.0%), nickel chloride (II) tetrahydrate ($NiCl_2·6H_2O$, ≥99.0%), and copper (II) chloride dihydrate ($CuCl_2·2H_2O$, ≥99.0%) were bought from Sinopharm Chemical Reagent. 1,4-benzendicarboxylic acid (1,4-BDC, >99.0%) and triethylamine (TEA, >99.0%) were purchased from TCI. Potassium hydroxide (KOH, 99.99%), ethanol (CH_3CH_2OH, 99.5%) and N, N-dimethylformamide (DMF, 99.9%) were bought from Aladdin Reagent. Nafion solution (5 wt%) and ruthenium oxide (RuO_2) were obtained from Alfa Aesar. All chemicals were used directly without further purification. Ultrapure water (18 MΩ cm^{-1}) used in the experiments was supplied by a Millipore System (Millipore Q).

Synthesis of HE-MOF-RT

First, $MnCl_2·4H_2O$ (0.15 mmol, 29.7 mg), $FeCl_3·6H_2O$ (0.15 mmol, 40.5 mg), $CoCl_2·6H_2O$ (0.15 mmol, 35.7 mg), $NiCl_2·6H_2O$ (0.15 mmol, 35.7 mg) and $CuCl_2·2H_2O$ (0.15 mmol, 25.6 mg) were dissolved in a solution containing DMF (32 mL), ethanol (2 mL) and water (2 mL) under magnetic stirring. Next, 1,4-BDC (0.75 mmol, 124.6 mg) was added into the above solution. After 1,4-BDC was dissolved, 0.8mL TEA was quickly injected into the solution. Then, the solution was stirred for 5 min to obtain a uniform colloidal suspension. Afterwards, the colloidal solution was continuously ultrasonicated for 1 h (40 kHz) under airtight conditions. Finally, the product was collected via centrifugation and washed with water and ethanol before drying at 60 °C.

Synthesis of HE-MOF-ST

First, $MnCl_2·4H_2O$ (0.15 mmol, 29.7 mg), $FeCl_3·6H_2O$ (0.15 mmol, 40.5 mg), $CoCl_2·6H_2O$ (0.15 mmol, 35.7 mg), $NiCl_2·6H_2O$ (0.15 mmol, 35.7 mg) and $CuCl_2·2H_2O$ (0.15 mmol, 25.6 mg) were dissolved in a solution containing DMF (32 mL), ethanol (2 mL) and water (2 mL) under magnetic stirring. Next, 1,4-BDC (0.75 mmol, 124.6 mg) was added into the above solution. After 1,4-BDC was dissolved, the homogeneous solution was transferred to a 50 mL Teflon-

lined stainless steel autoclave at 140 °C for 48 h under airtight conditions. Finally, the product was collected via centrifugation and washed with water and ethanol before drying at 60 °C.

Scale-up synthesis of HE-MOF-RT

In a 2000 mL beaker, $MnCl_2·4H_2O$ (6 mmol, 1.19 g), $FeCl_3·6H_2O$ (6 mmol, 1.62 g), $CoCl_2·6H_2O$ (6 mmol, 1.43 g), $NiCl_2·6H_2O$ (6 mmol, 1.43 g) and $CuCl_2·2H_2O$ (6 mmol, 1.02 g) were dissolved in a solution containing DMF (1280 mL), ethanol (80 mL) and water (80 mL) under magnetic stirring. Next, 1,4-BDC (30 mmol, 4.98 g) was added into the above solution. After 1,4-BDC was dissolved, 32 mL TEA was quickly injected into the solution. Then, the solution was stirred for 5 min to obtain a uniform colloidal suspension. Afterwards, the colloidal solution was continuously ultrasonicated for 1 h (40 kHz) under airtight conditions. Finally, the product was collected via centrifugation and washed with water and ethanol before drying at 60 °C.

Synthesis of bimetallic NiM-MOFs (M = Mn, Fe, Co and Cu)

For NiMn-MOF, $NiCl_2·6H_2O$ (0.375 mmol, 89.1 mg) and $MnCl_2·4H_2O$ (0.375 mmol, 74.2 mg) were first dissolved in a solution containing DMF (32 mL), ethanol (2 mL) and water (2 mL) under magnetic stirring. Next, 1,4-BDC (0.75 mmol, 124.6 mg) was added into the above solution. After 1,4-BDC was dissolved, 0.8mL TEA was quickly injected into the solution. Then, the solution was stirred for 5 min to obtain a uniform colloidal suspension. Afterwards, the colloidal solution was continuously ultrasonicated for 1 h (40 kHz) under airtight conditions. Finally, the product was collected via centrifugation and washed with water and ethanol before drying at 60 °C. The synthesis steps of NiFe-MOF, NiCo-MOF and NiCu-MOF are same to NiMn-MOF except 0.375 mmol of $MnCl_2·4H_2O$ was replaced by 0.375 mmol of $FeCl_3·6H_2O$, $CoCl_2·6H_2O$ and $CuCl_2·2H_2O$, respectively.

Synthesis of trimetallic NiCoM-MOFs (M = Mn, Fe and Cu)

For NiCoMn-MOF, $NiCl_2·6H_2O$ (0.25 mmol, 59.4 mg), $CoCl_2·6H_2O$ (0.25 mmol, 59.5 mg) and $MnCl_2·4H_2O$ (0.25 mmol, 49.5 mg) were first dissolved in a solution containing DMF (32 mL), ethanol (2 mL) and water (2 mL) under magnetic stirring. Next, 1,4-BDC (0.75 mmol, 124.6 mg) was added into the above solution. After 1,4-BDC was dissolved, 0.8mL TEA was quickly

injected into the solution. Then, the solution was stirred for 5 min to obtain a uniform colloidal suspension. Afterwards, the colloidal solution was continuously ultrasonicated for 1 h (40 kHz) under airtight conditions. Finally, the product was collected via centrifugation and washed with water and ethanol before drying at 60 °C. The synthesis steps of NiCoFe-MOF and NiCoCu-MOF are same to NiCoMn-MOF except 0.25 mmol of $MnCl_2·4H_2O$ was replaced by 0.25 mmol of $FeCl_3·6H_2O$ and $CuCl_2·2H_2O$, respectively.

Characterizations

The X-ray powder diffraction (XRD) patterns of the samples were recorded using an X-ray diffractometer (Rigaku D/Max-2500) using Cu Kα as X-ray radiation (λ = 1.5418 Å) under 40 kV and 30 mA. Data were collected in Bragg-Brettano mode using 0.02° divergence with a scan rate of 2° min^{-1}. N_2 adsorption-desorption isotherms of the samples were measured at 77 K using Belsorp-Mini II (BEL Japan Inc., Japan). Prior to the measurements, the samples were outgassed under vacuum for 10 h at 100 °C. The element analysis was conducted by inductively coupled plasma atomic emission spectrometry (ICP-AES, Agilent Technologies 700 Series). The scanning electron microscope (SEM) images, scanning electron microscope-energy dispersive X-ray spectroscopy (SEM-EDS) spectra and elemental mapping images of the samples were acquired using a Hitachi SU 8010 field emission scanning electron microscope coupled with energy dispersive X-ray spectroscopy operated at 15.0 kV. The transmission electron microscope (TEM) patterns were carried out using a Hitachi HT-7700 transmission electron microscope at 80.0 kV. The transmission electron microscope-energy dispersive X-ray spectroscopy (TEM-EDS) TEM-EDS analyses and elemental mapping were performed using a JEM-2010 transmission electron microscope coupled with energy dispersive X-ray spectroscopy. The samples were prepared by dropping catalyst powder dispersed in isopropanol onto carbon-coated copper TEM grids (Beijing Zhongxing Braim Technology Corp., China) using micropipettes and were dried under ambient conditions. X-ray photoelectron spectroscopy (XPS) was performed on the Thermo Scientific ESCALab 250Xi using 200 W monochromatic Al Kα radiation. The 500 μm X-ray spot was used for SAXPS analysis. The base pressure in the analysis chamber was about $3×10^{-9}$ mbar. Typically, the hydrocarbon C1s line at 284.8 eV from adventitious carbon is used for energy referencing in

XPS experiments.

Electrochemical measurements.

Electrochemical measurements were performed using a three-electrode system connected to an electrochemical workstation (CHI 660E). The working electrode was a glassy carbon electrode (GCE) (diameter: 3 mm, area: 0.07069 cm^2) from CH Instruments. Saturated calomel electrode (SCE) and graphite rod were used as reference and counter electrodes, respectively. The electrocatalytic activity of samples for OER was studied in O_2- saturated 1.0 M KOH (pH = 14) aqueous electrolyte. Unless otherwise stated, all experiments were performed at ambient temperature (23 ± 2 °C) and electrode potentials were converted to the RHE scale using E(RHE) = E(SCE) + 0.242 V + 0.059 * pH. All LSV data were collected for 90% *iR* drop compensation. The chronopotentionmetry test was carried out under the same experimental setup without the *iR* drop compensation. The electrochemical impedance spectra (EIS) experiments were recorded under an open-circuit voltage in the frequency range from 10^5 to 0.05 Hz.

Typically, 3 mg of catalyst powder was dispersed in 980 µL mixture of water and ethanol (1:3, v/v), and then 20 µL of Nafion solution (5 wt%) was added. The suspension was immersed in an ultrasonic bath for 30 min to prepare a homogeneous ink. The working electrode was prepared by depositing 5 µl catalyst ink onto GCE (catalyst loading 0.21 mg cm^{-2}). The catalyst inks were also loaded on carbon cloth (CC, WOS1009) electrode with same mass loading.

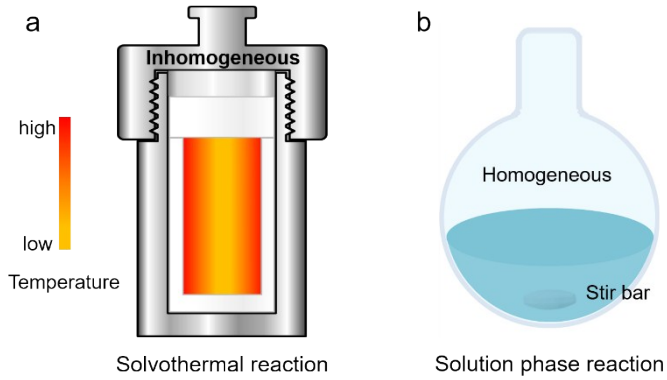

Figure S1. Illustration of the difference between a) solvothermal reaction and b) solution phase method. The thick stainless steel autoclave and Teflon lining prevent the fast heat transfer, resulting in inhomogeneous thermal distribution in the reaction system.[1] Without magnetic stirring, the solvothermal system also fail to hold a fast mass transfer. The above reasons lead to a non-uniform element distribution and bulky structure as discussed in characterization section. And it costs a lot to synthesize materials in large-scale by solvothermal reaction. In contrast, the solution phase method can hold better mass transfer and homogeneous thermal distribution (ambient temperature in our experiments) under fast magnetic stirring. The scale-up synthesis can simply be achieved by scaling up the reaction vessel.

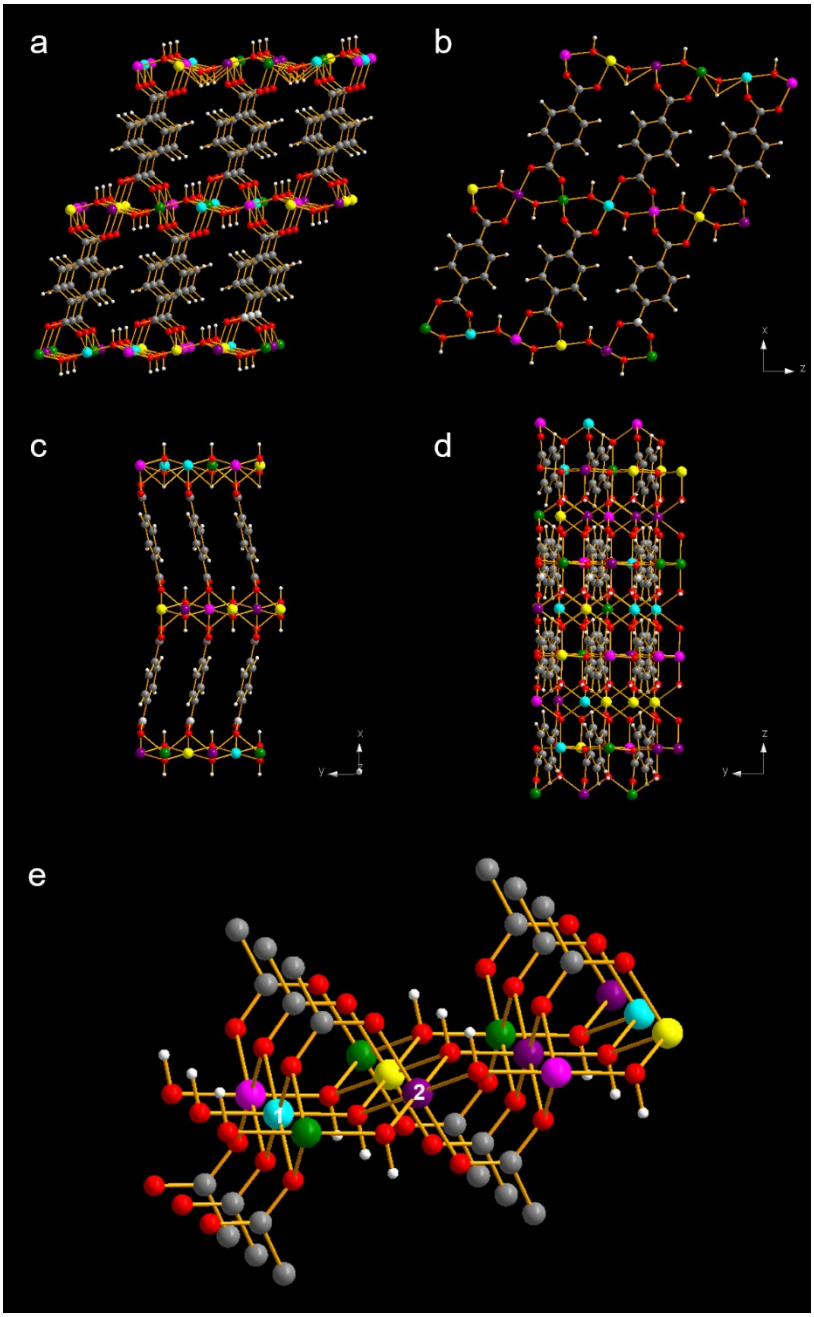

Figure S2. Crystal structure of HE-MOF-RT. a) Overall crystal structure of HE-MOF-RT with three coordination structural layers. b-d) Structure of a) viewed at different directions. e) Magnified crystal structure of HE-MOF-RT. Color scheme for chemical representation: pink for Mn, yellow for Fe, purple for Co, green for Ni, cyan for Co, red for O, grey for C and white for H. As for the ideal bulk crystal, the five metal atoms are octahedrally coordinated by six O atoms in two ways: (1) four O atoms from carboxylates and the other two from hydroxyls (e.g., marked as 1 in Figure S2e); or (2) two O atoms from carboxylates and the other four form hydroxyls (e.g., marked as 2 in Figure S2e).

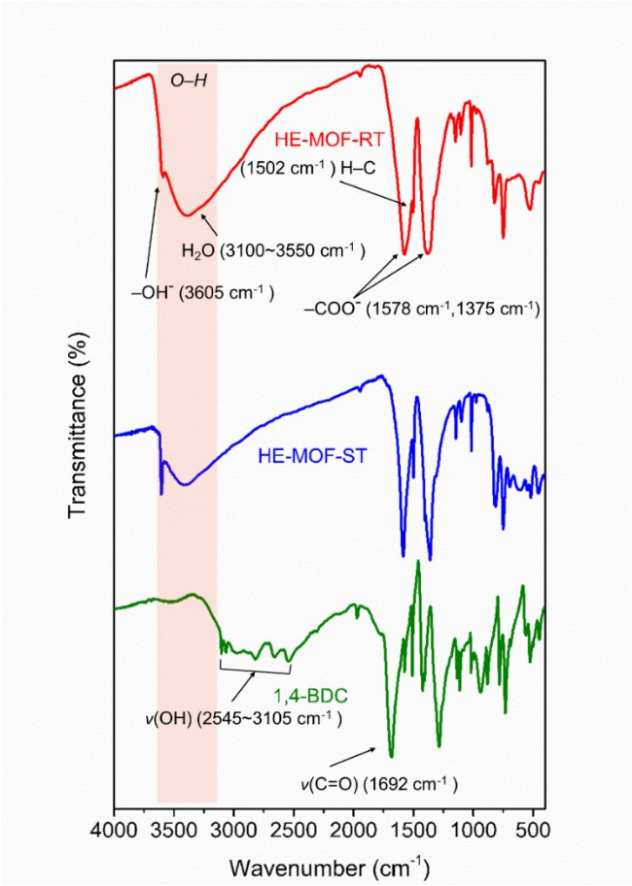

Figure S3. FT-IR spectra of HE-MOF-RT, HE-MOF-ST and 1, 4-BDC. For commercial 1,4-BDC, the characteristic band at 1692 cm^{-1} and the broad bands between 2545 cm^{-1} and 3105 cm^{-1} are attributed to ν(C=O) and ν(OH) of the non-ionic carboxyl (-COO) groups. For HE-MOF-RT, the characteristic band at 1502 cm^{-1}, 1578 cm^{-1} and 1375 cm^{-1} are assigned to the stretching vibrations of para-aromatic C-H group and the asymmetric and symmetric vibrations of the coordinated carboxyl ($-COO^-$) group, respectively. Obviously, the characteristic bands of original 1,4-BDC at 1692 cm^{-1} and 2545~3105 cm^{-1} disappear and new bands appear at 1502 cm^{-1}, 1578 cm^{-1} and 1375 cm^{-1} in the resulted HE-MOF-RT. These results indicate the deprotonation of acidic COOH after complexation with metal ions.[2, 3] Moreover, the characteristic band at 3605 cm^{-1} and the broad bands between 3100 cm^{-1} and 3550 cm^{-1} are attributed to the stretching vibrations of OH^- and water molecule, showing the presence of the coordinated $–OH^-$ and H_2O in HE-MOF-RT. These two separated modes confirm that –COO of 1,4-BDC is coordinated with metal ions in a bi-dentate mode.[4, 5] Here the characteristic bands of HE-MOF-ST are not discussed since they share almost same IR spectra (same peaks expect intensity) with HE-MOF-ST.

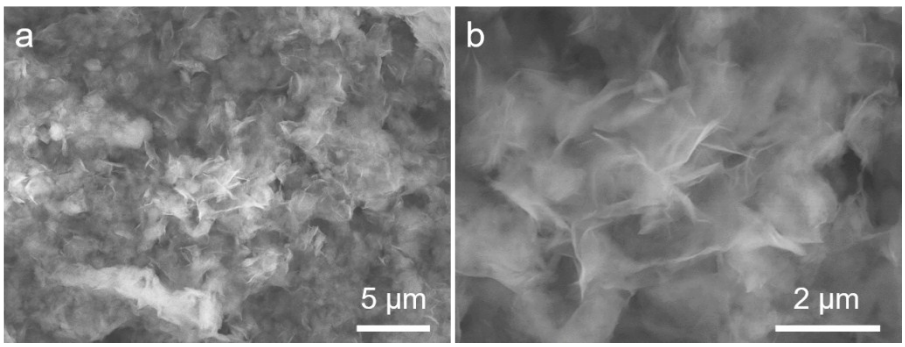

Figure S4. SEM images of HE-MOF-RT nanosheets. The ultrathin structure of HE-MOF-RT can be also discerned by SEM survey.

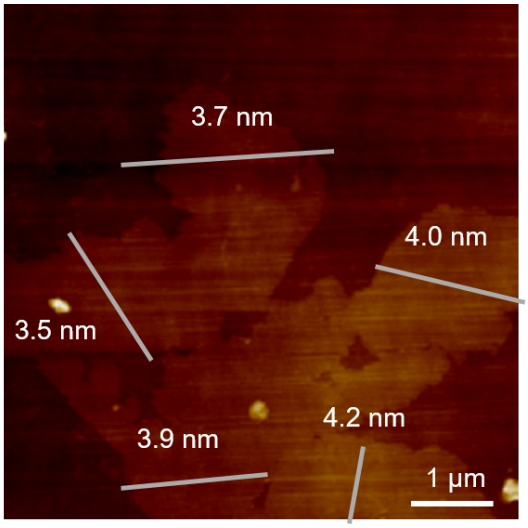

Figure S5. AFM image HE-MOF-RT nanosheets.

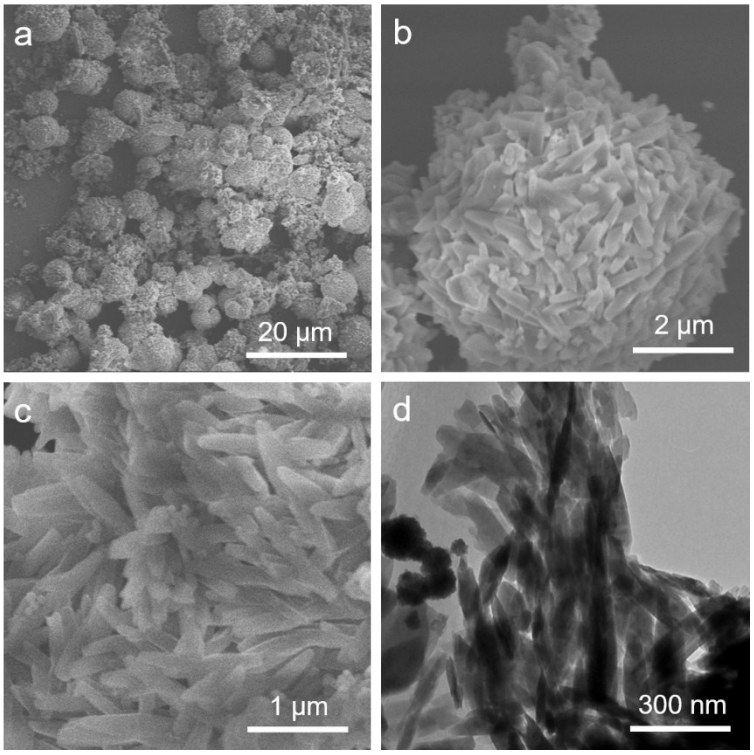

Figure S6. a-c) SEM images and d) TEM image of HE-MOF-ST.

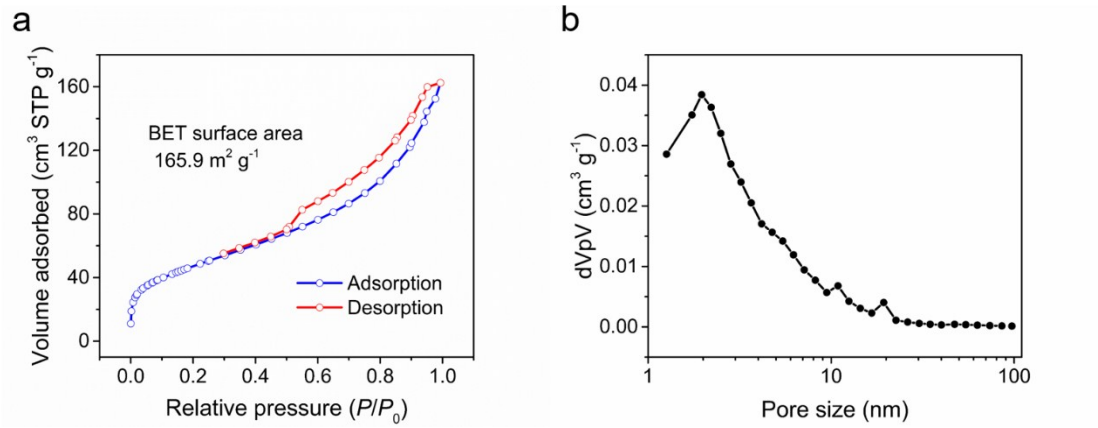

Figure S7. a) N_2 adsorption-desorption isotherm and b) the corresponding pore size distribution of HE-MOF-RT at 77 K. HE-MOF-RT has a relatively high BET surface area and possesses obvious mesoporous structure. According to the classification by IUPAC,[6] the isotherm of HE-MOF-RT nanosheets can be identified as type II with an identifiable H4-type hysteresis loop, which is associated with the slit-like pores formed by aggregation of nanosheets.[7]

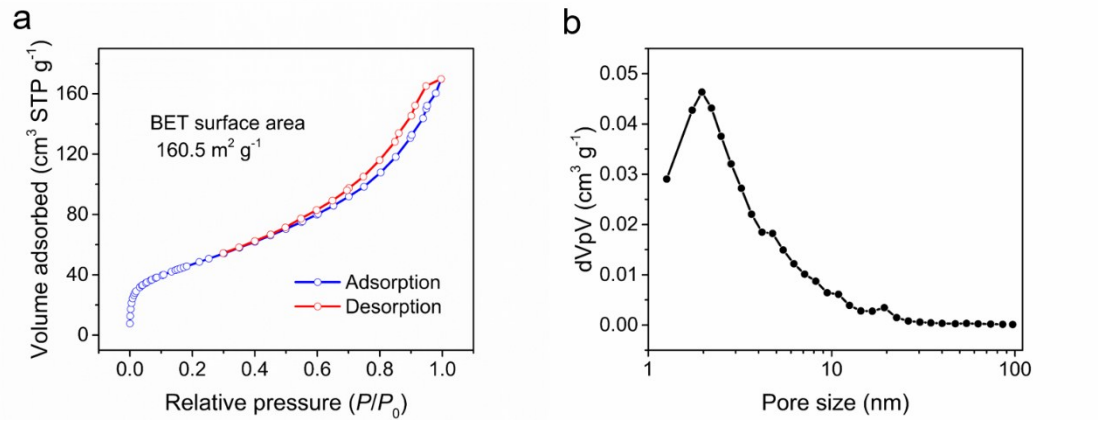

Figure S8. a) N_2 adsorption-desorption isotherm and b) the corresponding pore size distribution of Ni-MOF-RT at 77 K. Ni-MOF-RT also possesses a type II isotherm with an identifiable H4-type hysteresis loop. And the BET surface area of 160.5 m^2 g^{-1} is derived, originating from the slit-like pores formed by aggregation of nanosheets.

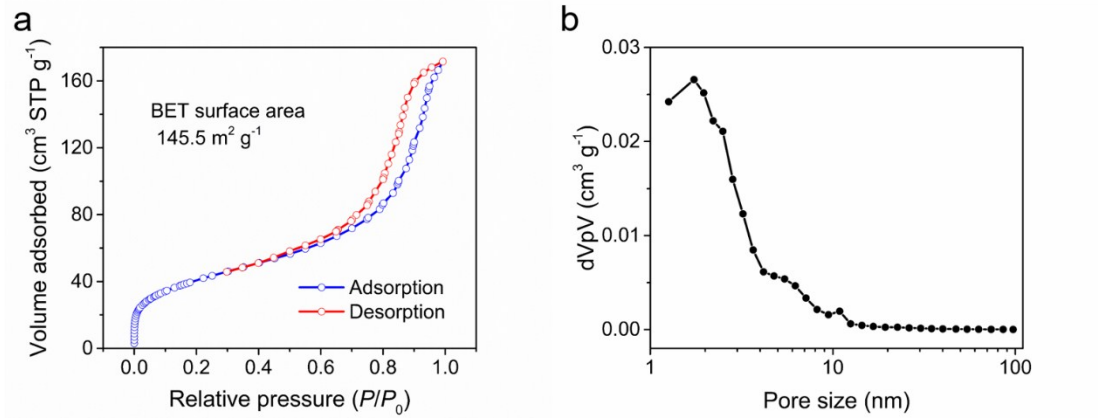

Figure S9. a) N_2 adsorption-desorption isotherm and b) the corresponding pore size distribution of HE-MOF-ST at 77 K.

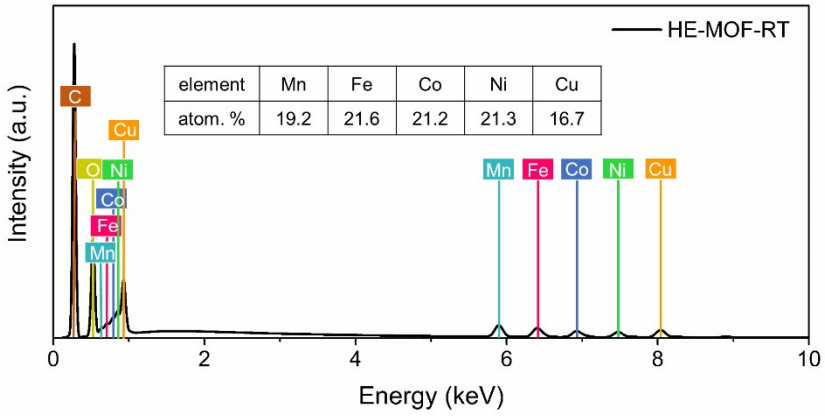

Figure S10. EDS spectrum of HE-MOF-RT, and the inserted table summarizes the atomic ratio of elements inside HE-MOF-RT. This result is in good agreement with the ICP results.

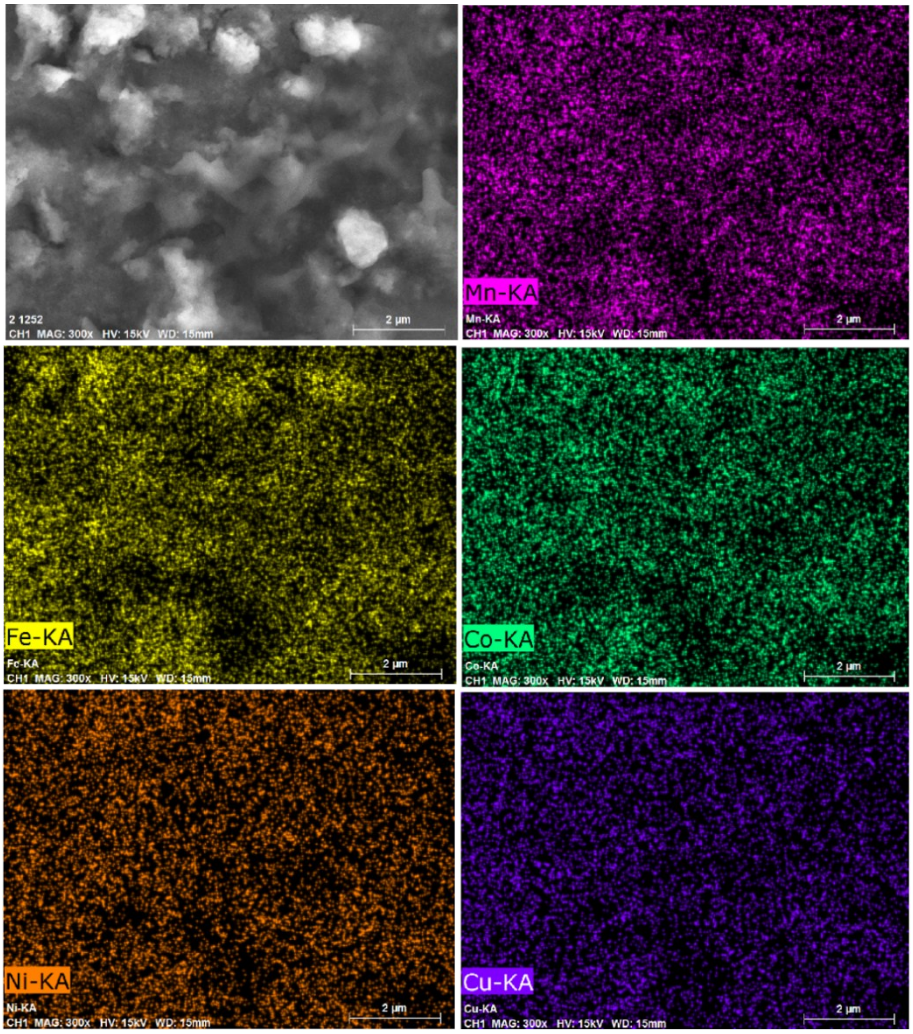

Figure S11. SEM-EDS mapping of HE-MOF-RT. Five metals are uniformly and randomly dispersed in the HE-MOF-RT sample.

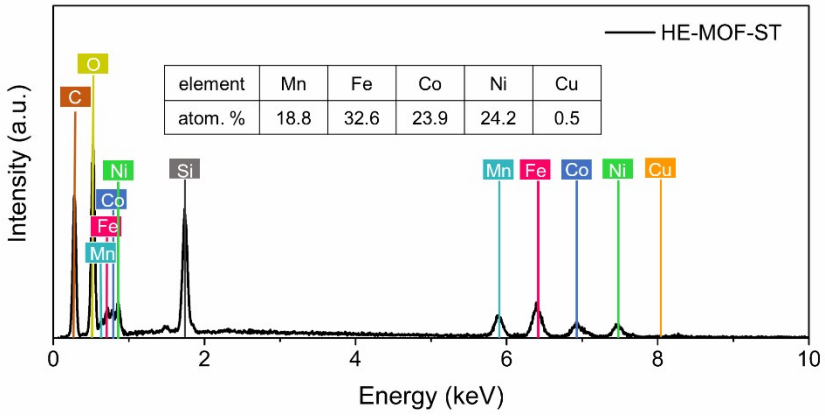

Figure S12. EDS spectrum of HE-MOF-RT, and the inserted table summarizes the atomic ratio of elements inside HE-MOF-RT. The Si signal is induced by the silicon wafer as SEM support. This result is in good agreement with the ICP results. The widely accepted concept of high entropy materials are defined as, "those composed of five or more principal elements with the concentration of each element being between 5 and 35 at.-%."[8] Accordingly, HE-MOF-ST cannot be regarded as high entropy materials.

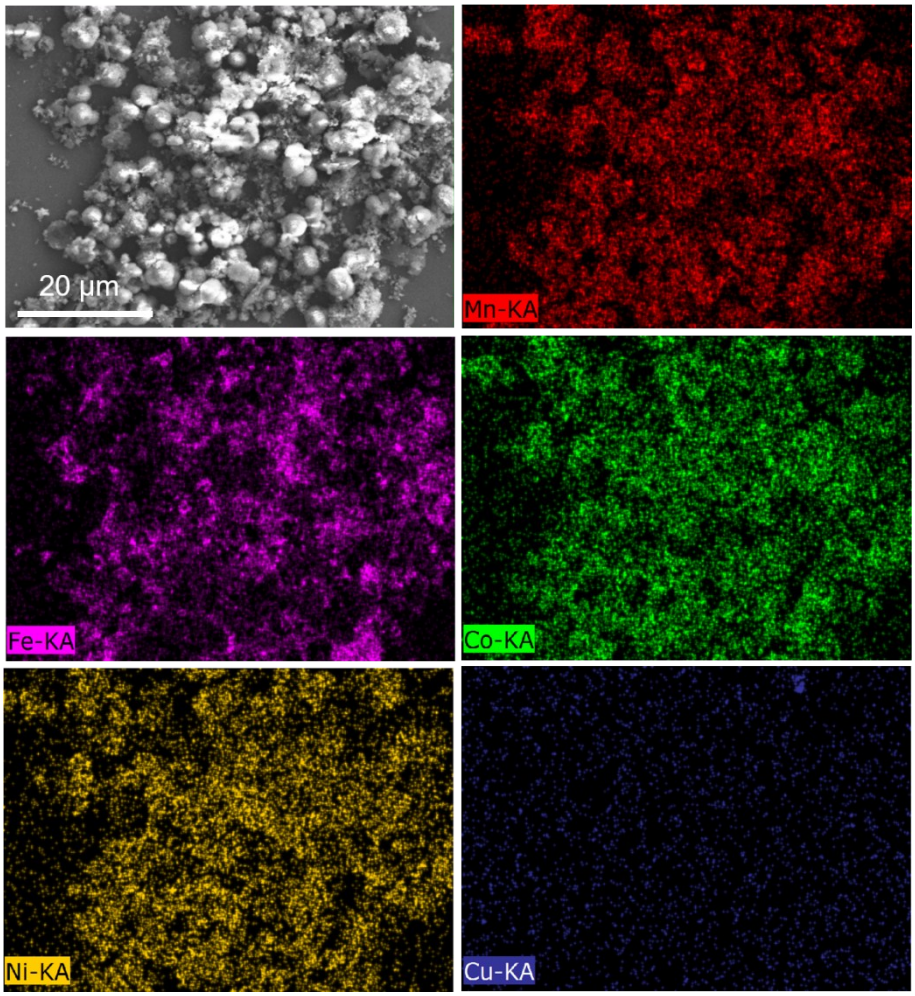

Figure S13. SEM-EDS mapping of HE-MOF-ST. Only Mn^{2+}, Ni^{2+} and Co^{2+} uniformly and randomly dispersed in HE-MOF-ST, while Fe^{3+} are clustered or segregated in the map. For the map of Cu, only background color is observed. Combining the analyses of XRD pattern, EDS spectrum and ICP result of HE-MOF-ST, we speculate that HE-MOF-ST is MOF composite contain four metal ions rather than HE-MOFs.

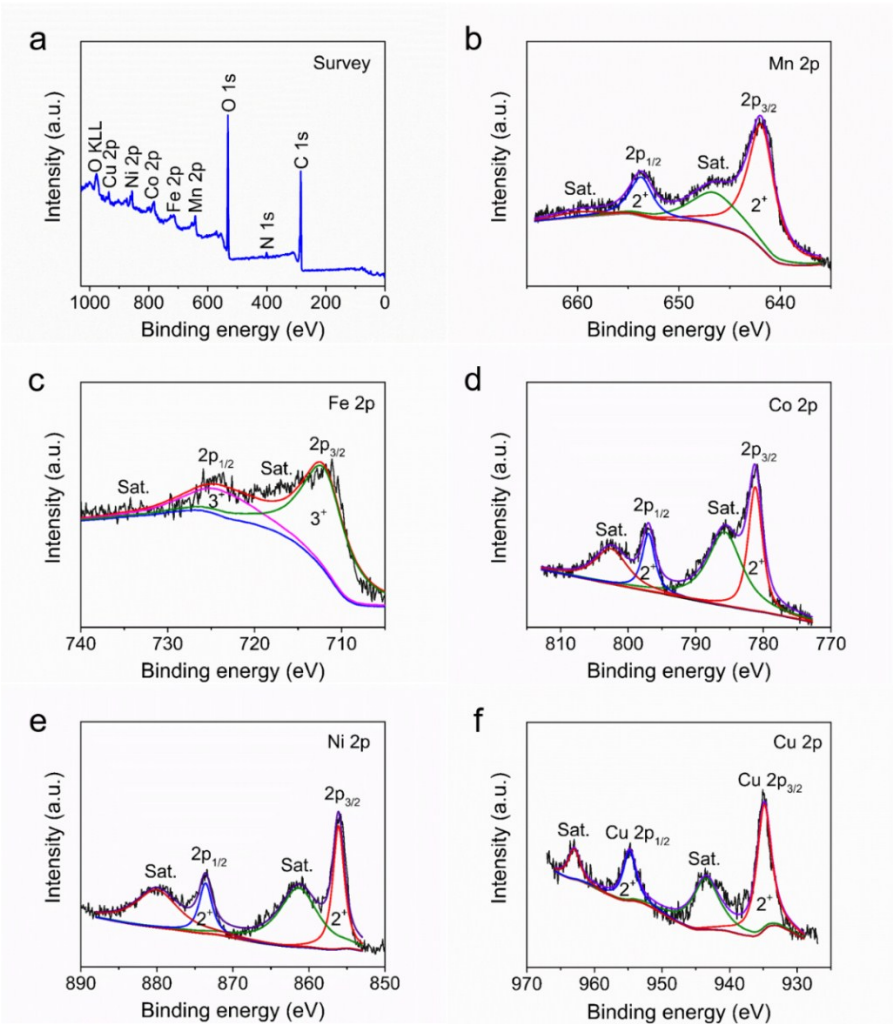

Figure S14. XPS spectra of a) survey, b) Mn 2p, c) Fe 2p, d) Co 2p, e) Ni 2p and f) Cu 2p of HE-MOF-RT. For Mn 2p spectrum, the peaks at 641.9 eV and 653.7 eV are attributed to Mn^{2+}, where peaks centered at 646.9 eV and 660.2 eV can be assigned to satellite peak for the above peaks. The high-resolution Fe 2p spectrum deconvolutes into two peaks at 712.5 eV and 725.1 eV, corresponding to Fe $2p_{3/2}$ and Fe $2p_{1/2}$, respectively, suggesting the exclusive Fe^{3+} oxidation state in the sample. In the high-resolution Co 2p spectrum, the peaks of Co $2p_{3/2}$ and Co $2p_{1/2}$ at 781.2 eV and 797.0 eV, along with two satellite peaks at 785.8 eV and 802.6 eV, demonstrate the existence of the +2 oxidation state of Co. In the high-resolution Ni 2p spectrum, the peaks of Ni $2p_{3/2}$ and Ni $2p_{1/2}$ at 856.1 eV and 873.5 eV, along with two satellite peaks at 861.5 eV and 880.1 eV, demonstrate the existence of the +2 oxidation state of Ni. The Cu 2p spectra show clear features representative of Cu^{2+} oxidation states, with binging energies at 934.8 eV (Cu $2p_{3/2}$) and 954.7 eV (Cu $2p_{1/2}$), respectively.

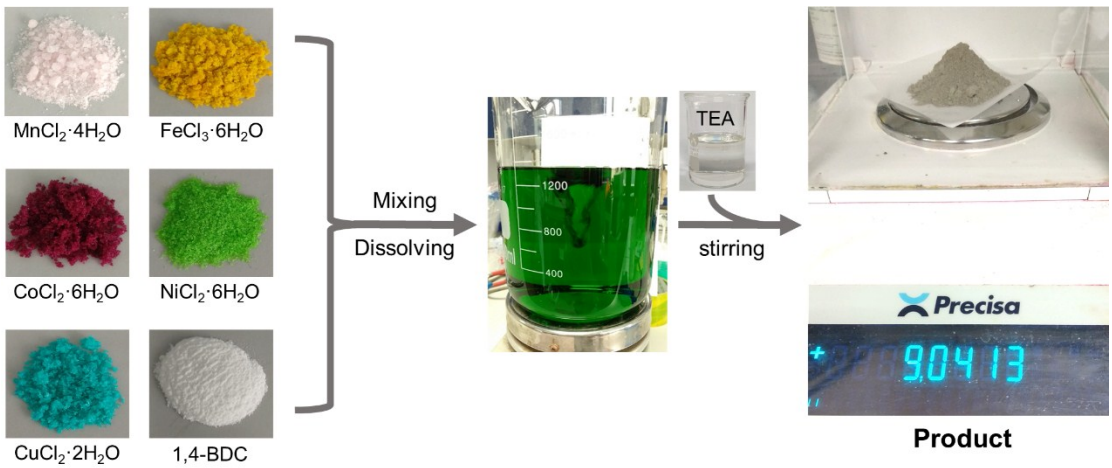

Figure S15. Scheme for a scale-up synthesis of HE-MOF-RT.

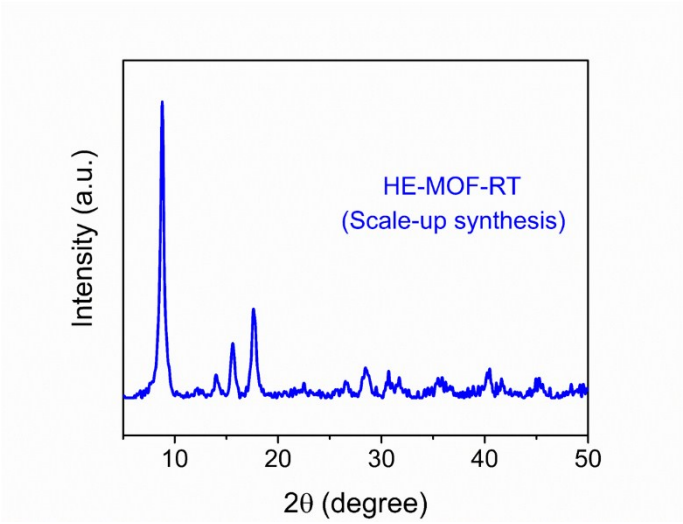

Figure S16. XRD pattern for HE-MOF-RT prepared in a scale-up synthesis. The product shares similar XRD pattern with HR-MOF-RT.

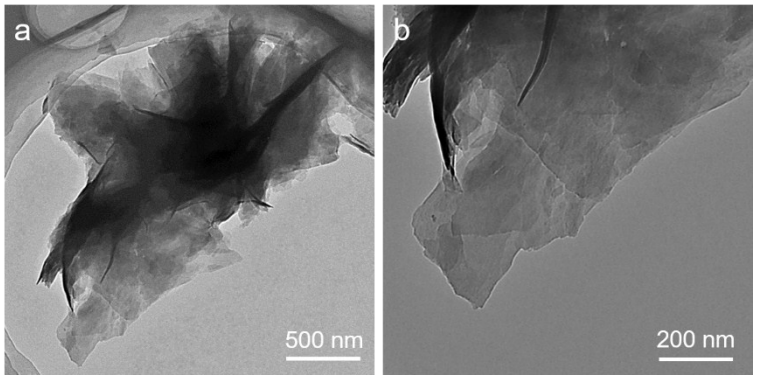

Figure S17. TEM image for HE-MOF-RT prepared in a scale-up synthesis. The product possesses ultrathin nanosheets structure with curly edges, which is similar to HE-MOF-RT.

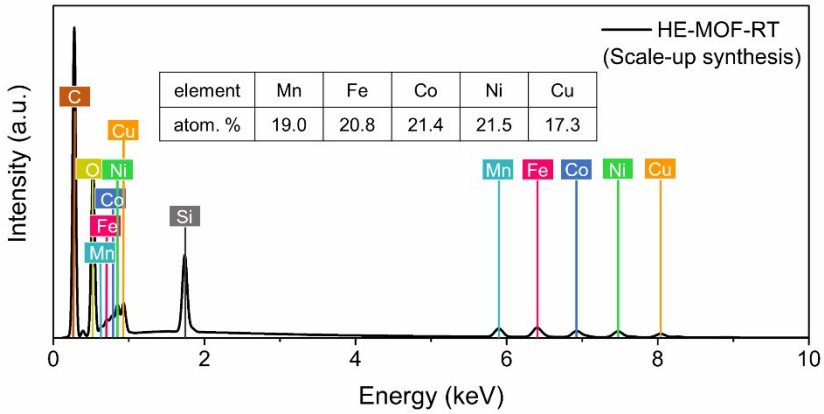

Figure S18. EDS spectrum for HE-MOF-RT prepared in a scale-up synthesis. The product shows a near-equimolar ratio with five metal species, suggesting the successful formation of HE-MOF material in scale-up synthesis.

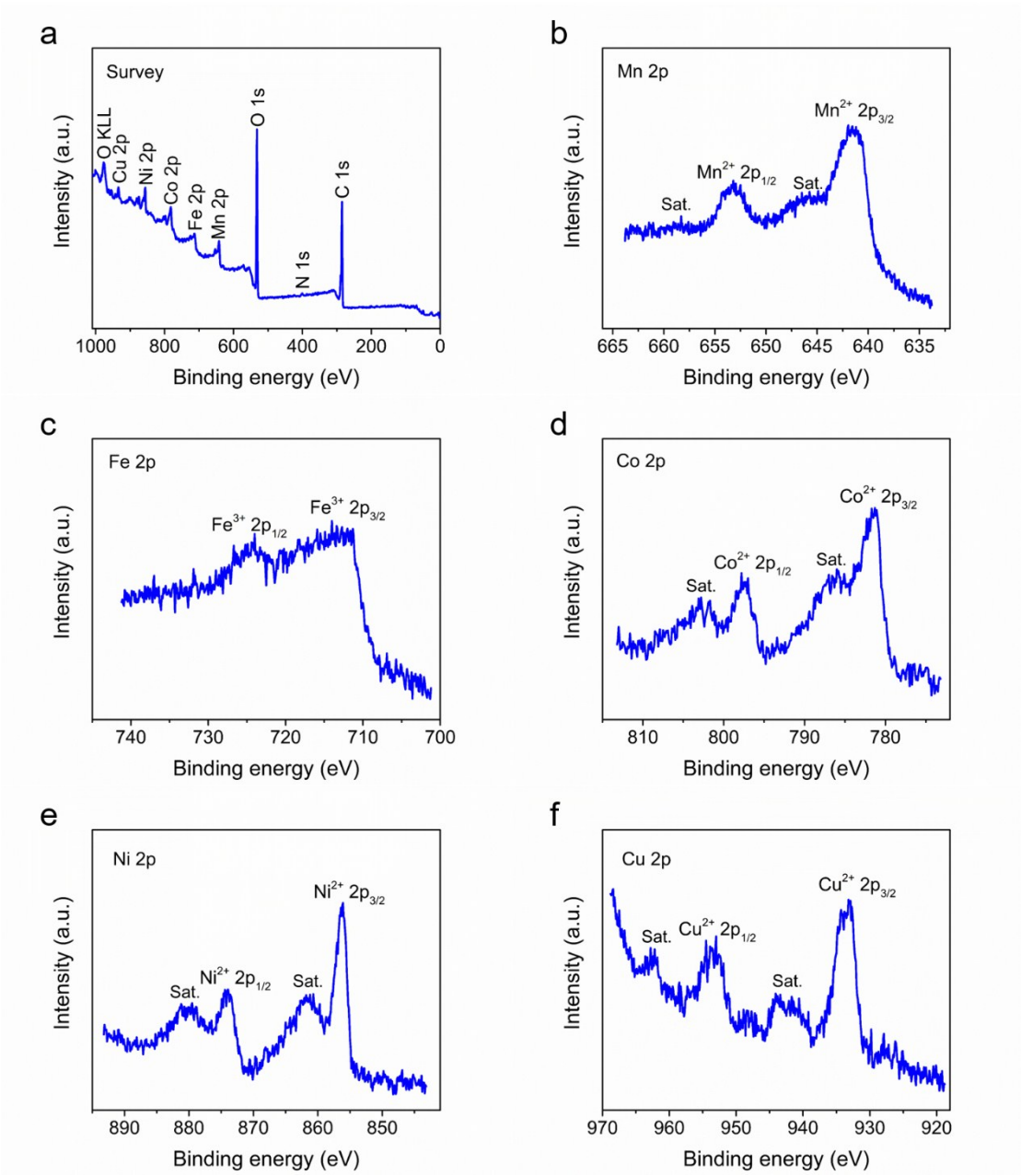

Figure S19. XPS spectra of a) survey, b) Mn 2p, c) Fe 2p, d) Co 2p, e) Ni 2p and f) Cu 2p of HE-MOF-RT prepared in a scale-up synthesis.

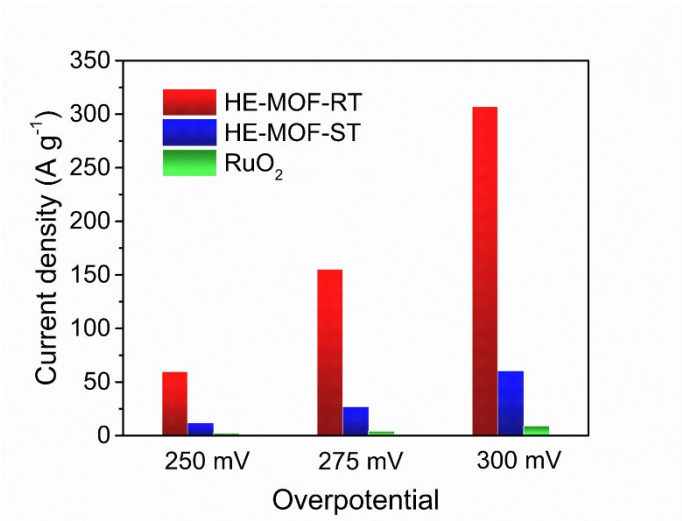

Figure S20. Mass activities of different catalysts at various applied potentials.

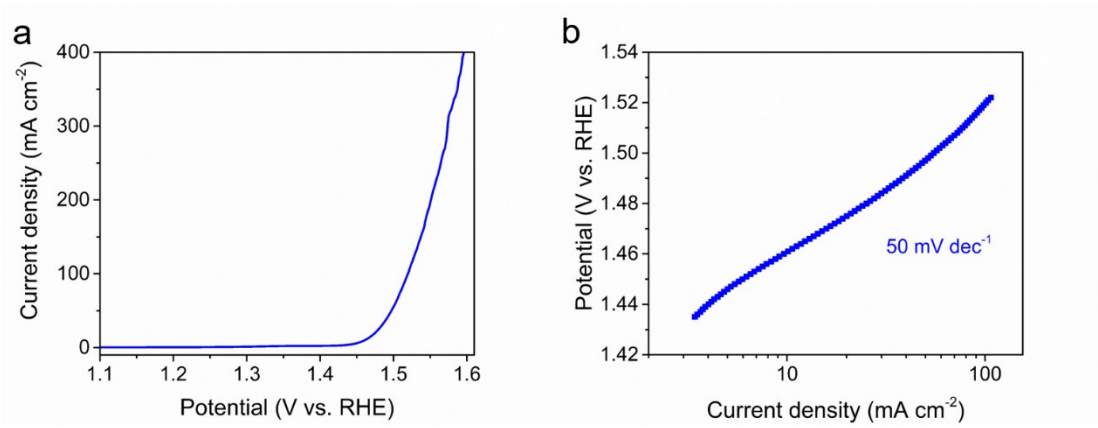

Figure S21. a) LSV curve and b) the corresponding Tafel plots of HE-MOF-RT on carbon cloth electrode.

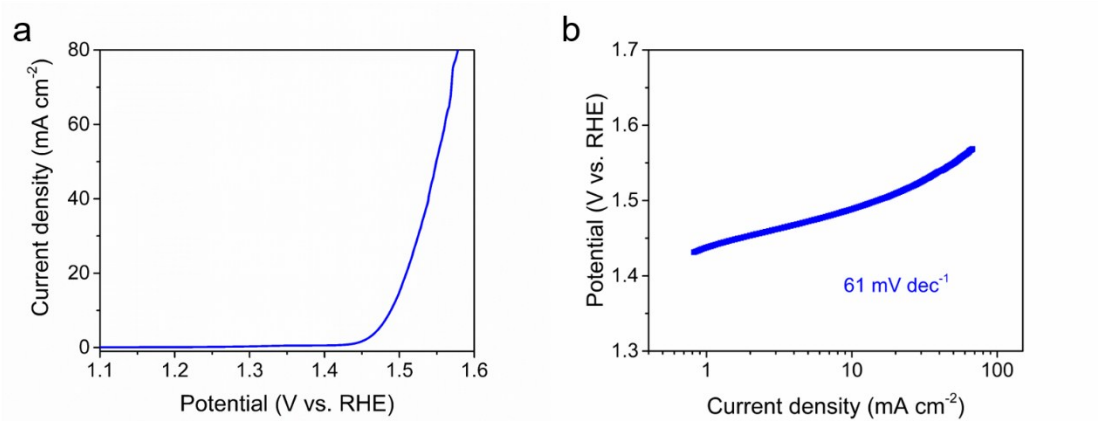

Figure S22. a) LSV curve and b) the corresponding Tafel plots of HE-MOF-RT prepared in a scale-up synthesis.

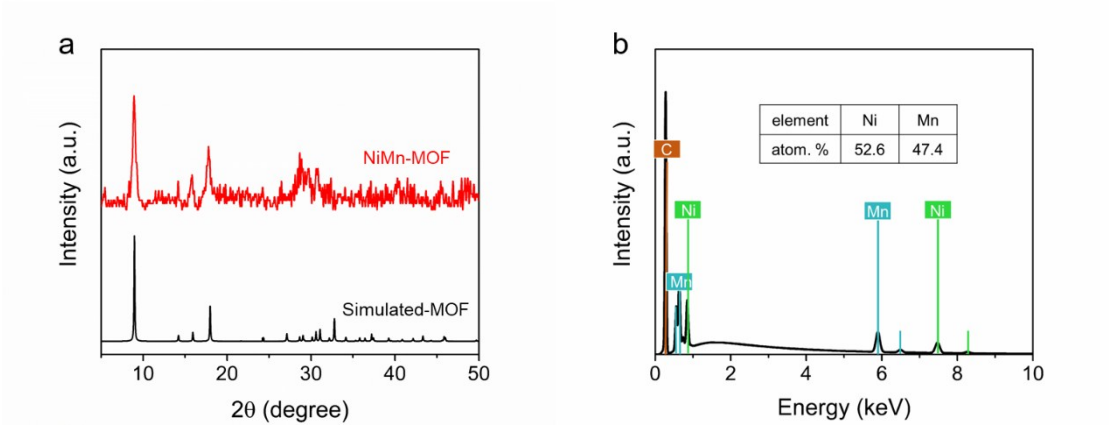

Figure S23. a) XRD pattern and b) EDS spectrum of NiMn-MOF synthesized by the solution phase method under ambient temperature.

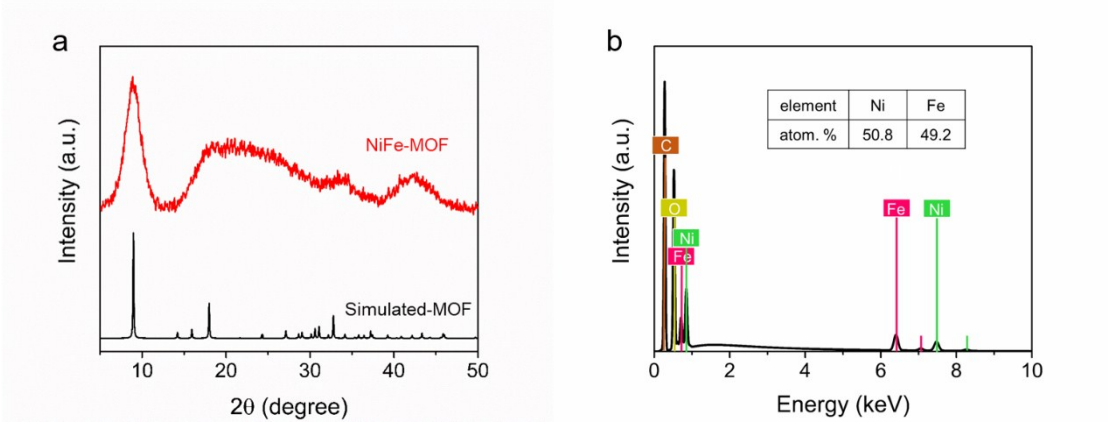

Figure S24. a) XRD pattern and b) EDS spectrum of NiFe-MOF synthesized by the solution phase method under ambient temperature.

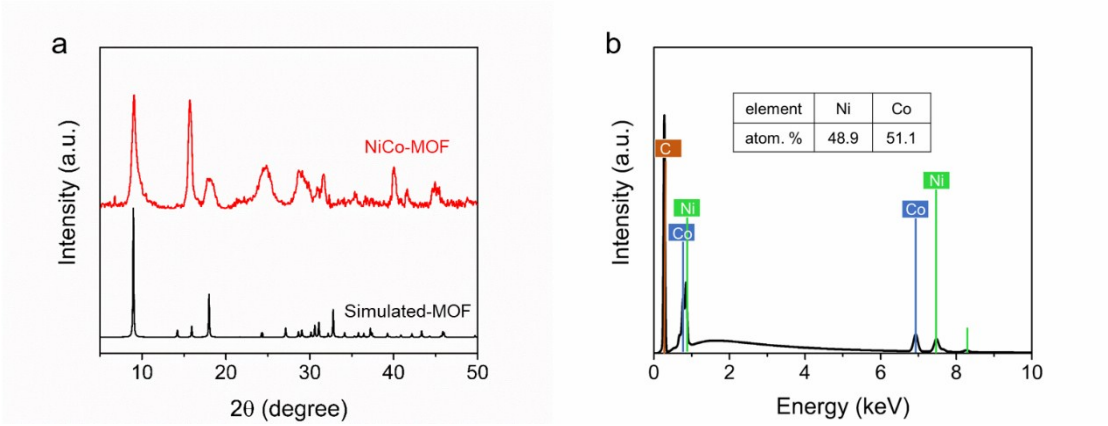

Figure S25. a) XRD pattern and b) EDS spectrum of NiCo-MOF synthesized by the solution phase method under ambient temperature.

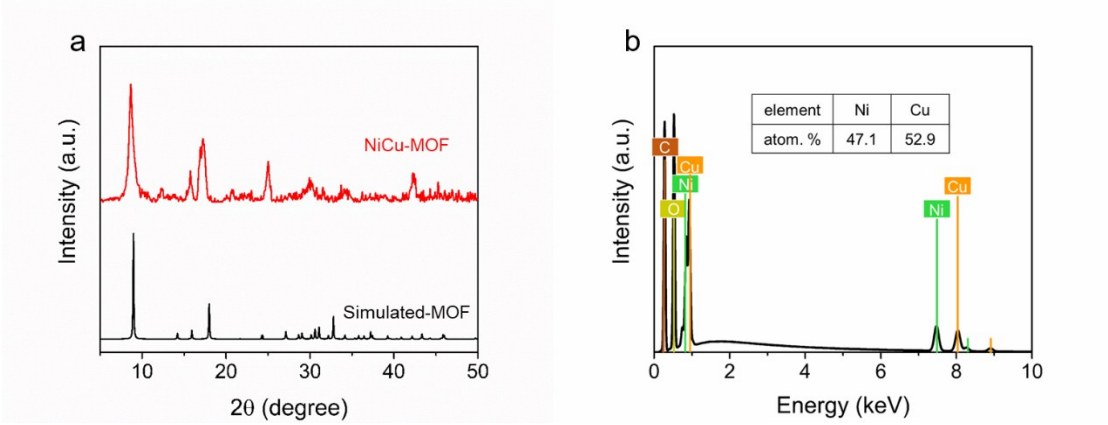

Figure S26. a) XRD pattern and b) EDS spectrum of NiCu-MOF synthesized by the solution phase method under ambient temperature.

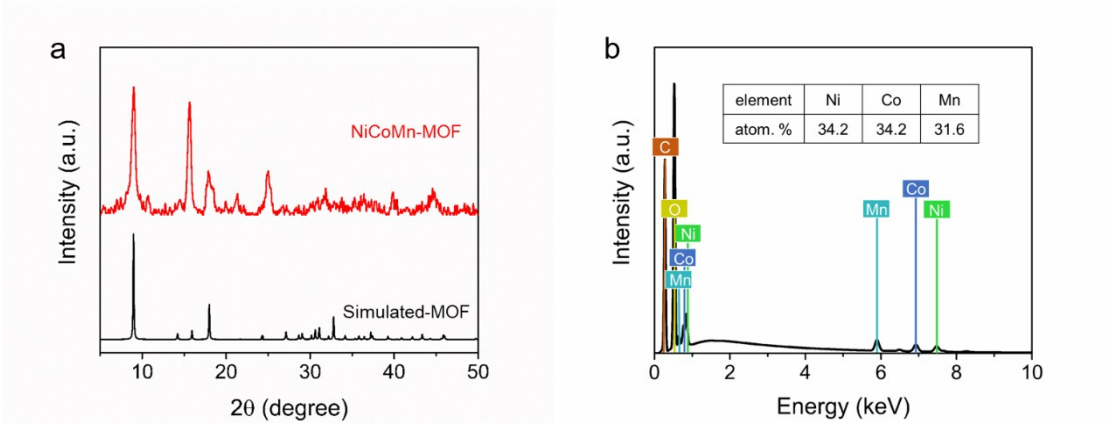

Figure S27. a) XRD pattern and b) EDS spectrum of NiCoMn-MOF synthesized by the solution phase method under ambient temperature.

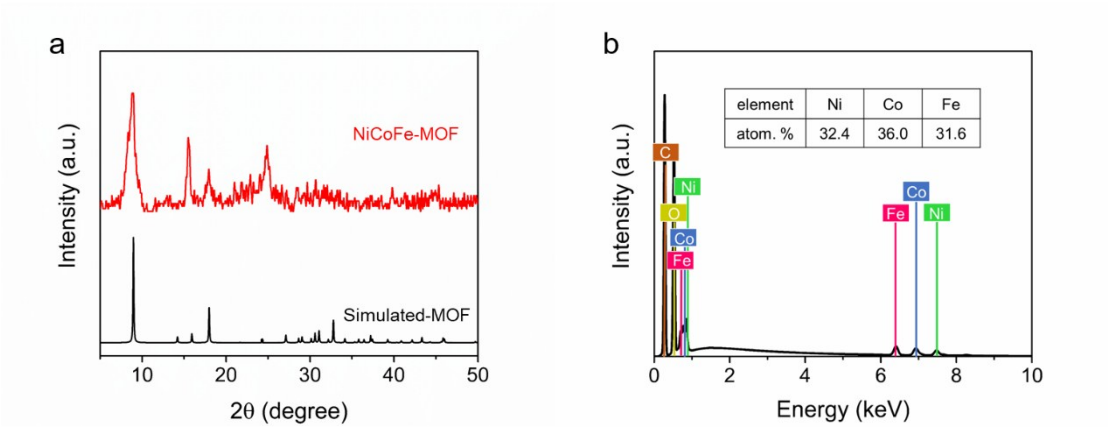

Figure S28. a) XRD pattern and b) EDS spectrum of NiCoFe-MOF synthesized by the solution phase method under ambient temperature.

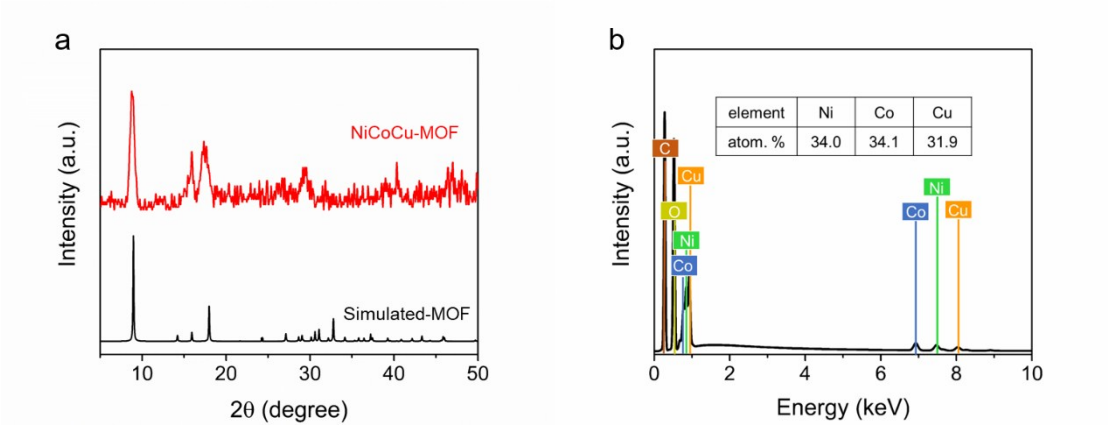

Figure S29. a) XRD pattern and b) EDS spectrum of NiCoCu-MOF synthesized by the solution phase method under ambient temperature.

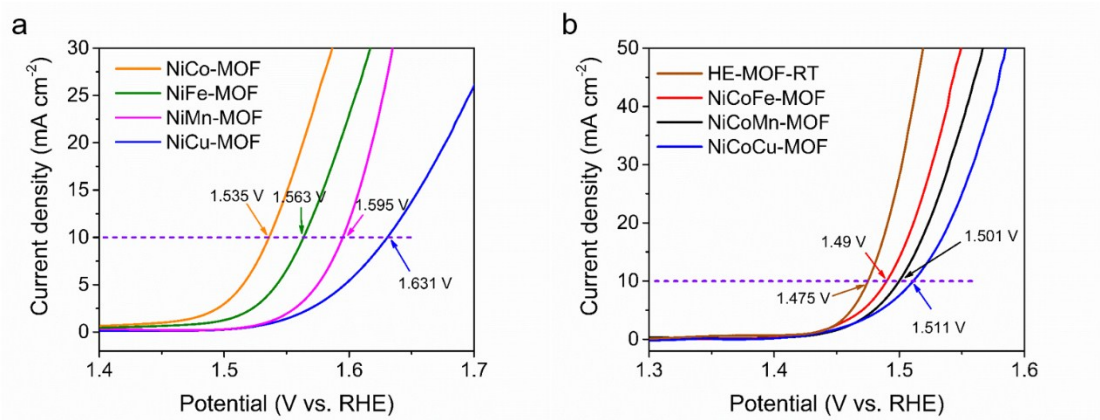

Figure S30. LSV polarization curves of a) bimetallic MOFs and b) trimetallic MOFs in 1 M KOH with a scan rate of 5 mV s^{-1}. The dotted horizontal line is a guide to the eye showing a current density of 10 mA cm^{-2}.

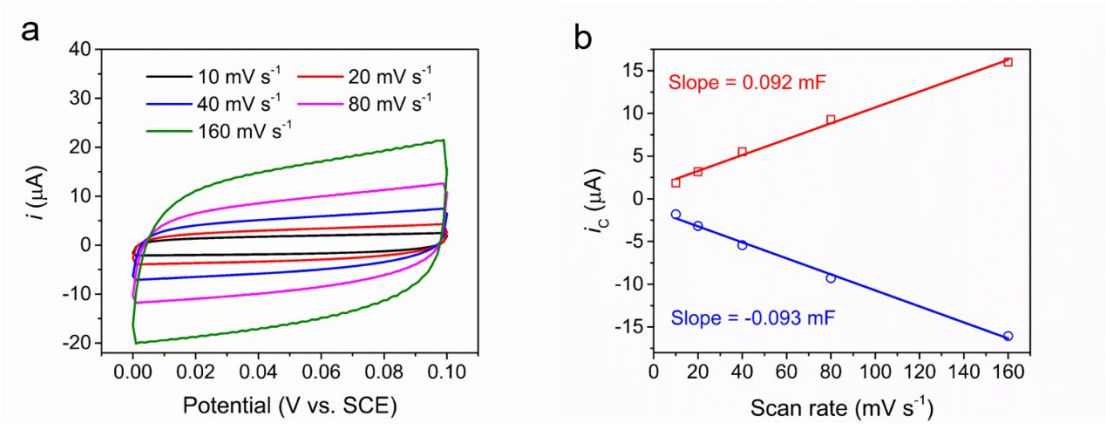

Figure S31. Double-layer capacitance measurements for determining electrochemically active surface area for HE-MOF-RT catalyst from voltammetry in 1 M KOH. a) Cyclic voltammograms were measured in a non-Faradaic region of the voltammogram at the following scan rate: 10, 20, 40, 80, 160 mV s^{-1}. b) The anodic (red open circle) and cathodic (blue open square) charging currents measured at -0.05 V vs. SCE plotted as a function of scan rate. The determined double-layer capacitance of the system is taken as the average of the absolute value of the slope of the linear fits to the data.

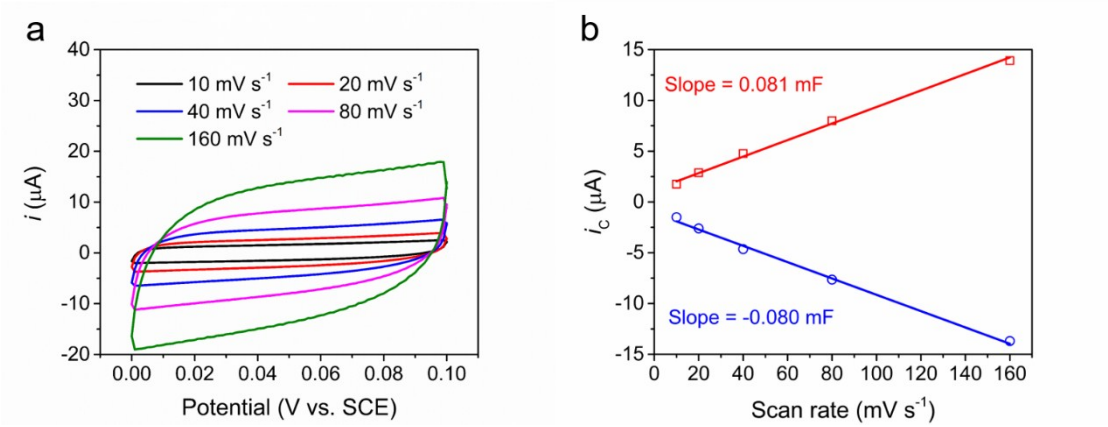

Figure S32. Double-layer capacitance measurements for determining electrochemically active surface area for HE-MOF-ST catalyst from voltammetry in 1 M KOH. a) Cyclic voltammograms were measured in a non-Faradaic region of the voltammogram at the following scan rate: 10, 20, 40, 80, 160 mV s^{-1}. b) The anodic (red open circle) and cathodic (blue open square) charging currents measured at -0.05 V vs. SCE plotted as a function of scan rate. The determined double-layer capacitance of the system is taken as the average of the absolute value of the slope of the linear fits to the data.

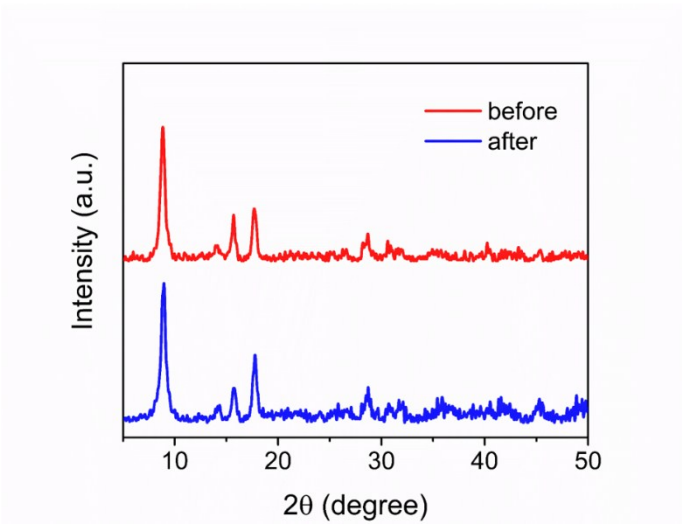

Figure S33. XRD pattern of HE-MOF-RT after stability test.

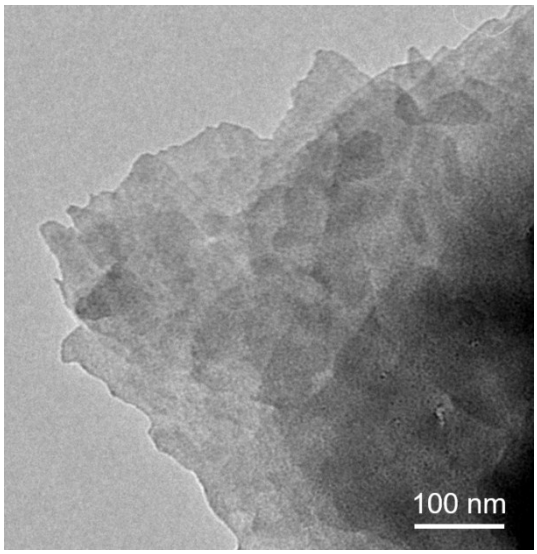

Figure S34. TEM image of HE-MOF-RT after stability test.

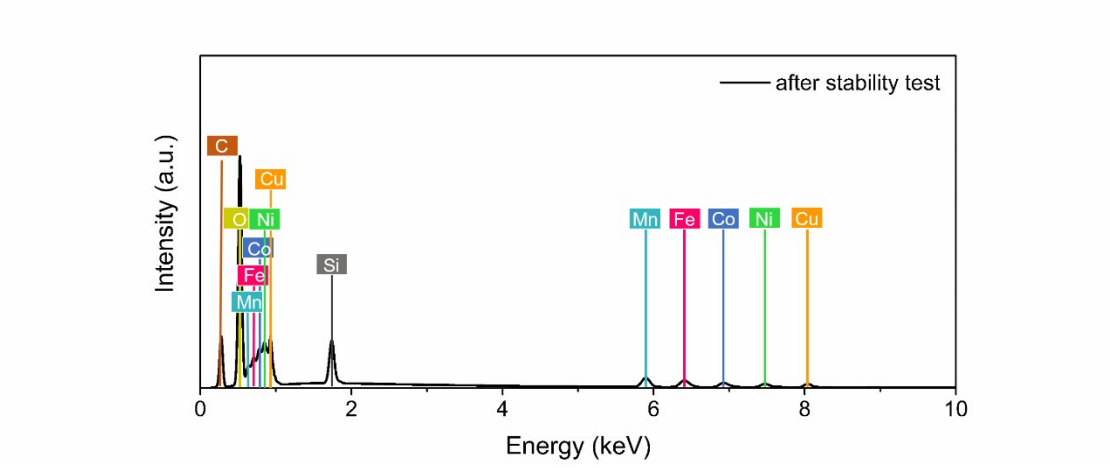

Figure S35. EDS spectrum of HE-MOF-RT after stability test.

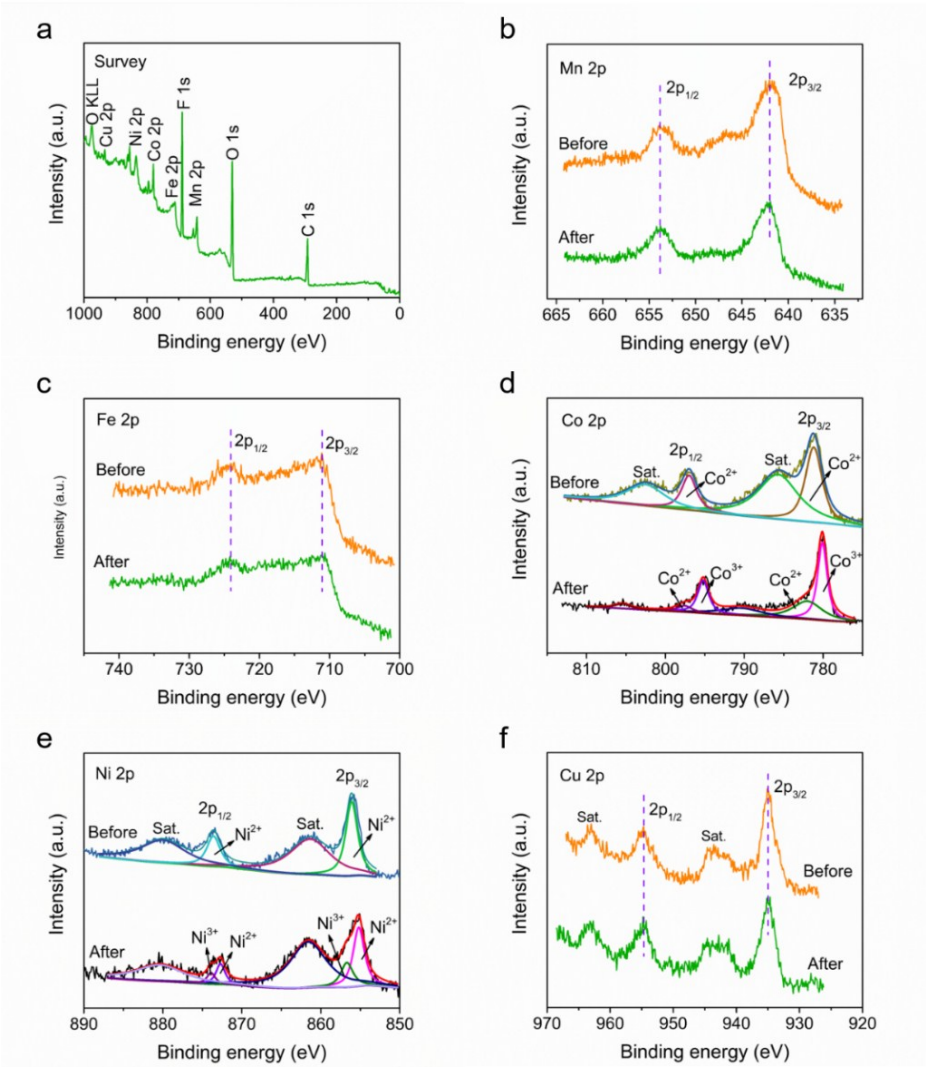

Figure S36. XPS spectra of a) survey, b) Mn 2p, c) Fe 2p, d) Co 2p, e) Ni 2p and f) Cu 2p of HE-MOF-RT after stability test. For survey spectrum, the observed F 1s peak is induced by Nafion used as binder for electrode preparation. Importantly, the characteristic peaks of Ni $2p_{3/2}$ and Ni $2p_{1/2}$ are shifted to lower binding energy after stability test. This result can be ascribed to altered local electronic structure of Ni atom after the degradation of organic ligand. The fitted peaks of Ni^{2+} (centered at 855.3 and 872.6 eV) along with their satellite are assigned to NiO.[9, 10] And two new peaks of Ni^{3+} at 856.7 eV and 873.9 eV are observed, which confirm the electrochemically formed NiOOH during water oxidation.[11] Similarity, the Co 2p spectrum also share same variation trend, confirming the formation of CoO and CoOOH during electrocatalytic process. For Mn, Fe and Cu, their XPS spectra are nearly identical to the pristine one before stability test. Indeed, it is noticeable that the chemical environment of Ni/Co-based active centers barely changed since they still bonded to six O atoms in NiO/CoO.

Table S1. Content of five metal species in HE-MOF-RT and HE-MOF-ST. The percentages of metals in each catalyst are determined by ICP-AES analyses.

Sample	Mn (atom.%)	Fe (atom.%)	Co (atom.%)	Ni (atom.%)	Cu (atom.%)
HE-MOF-RT	18.9	21.5	21.3	21.8	16.5
HE-MOF-ST	14.2	33.0	27.0	25.1	0.7

Table S2. Atomic ratio of five metal elements in HE-MOF-RT and HE-MOF-ST extracted from XPS spectra.

Sample	Mn (atom.%)	Fe (atom.%)	Co (atom.%)	Ni (atom.%)	Cu (atom.%)
HE-MOF-RT	19.2	21.0	20.8	22.0	17.0
HE-MOF-ST	13.9	32.1	28.8	24.1	1.1

Table S3. Comparisons of OER performance for recently reported transition metal-based electrocatalysts in 1.0 M KOH electrolyte.

Catalyst	Substrate	η (mV) at 10 mA cm^{-2}	Tafel slope (mV dec^{-1})	References
HE-MOF-RT	GCE	245	54	This work
HE-MOF-RT	carbon cloth	230	50	This work
Mn_3N_2	Ni foam	270	101	*Angew. Chem. Int. Ed.* 2018, 57, 698
Fe-Ni@NC-CNTs	GCE	274	45.47	*Angew. Chem. Int. Ed.* 2018, 57, 8921
NH_2MIL-88B(Fe_2Ni)-MOF	Ni foam	240	58.8	*Adv. Energy Mater.* 2018, 8, 1801065
Ni-MOF@Fe-MOF	GCE	265	82.0	*Adv. Funct. Mater.* 2018, 28, 1801554
CoFe-MOF-74	GCE	280	56	*ACS Energy Lett.* 2018, 3, 10, 2520
Fe–Co–P	GCE	252	33	*ACS Nano* 2018, 12, 158
CoO hexagrams	GCE	269	64.4	*Chem. Sci.* 2018, 9, 6961
CoP/NCNHP	GCE	310	70	*J. Am. Chem. Soc.* 2018, 140, 2610
$(Ni_2Co_1)_{0.925}Fe_{0.075}$-MOF	GCE	257	41.3	*Adv. Mater.* 2019, 31, 1901139

Cr-doped FeNi–P/NCN	GCE	240	72.36	*Adv. Mater.* 2019, 31, 1900178
Ni_3S_4-8-Ni-MOF@50	Ni foam	257	------	*Adv. Funct. Mater.* 2019, 29, 1900315
Cu_3N	Ni foam	286	118	*ACS Energy Lett.* 2019, 4, 747
Fe_1Ni_2-BDC-MOF	GCE	260	35	*ACS Energy Lett.* 2019, 4, 285
S|NiN_x–PC/EG	graphite foil	280	45	*Nat. Commun.* 2019, 10, 1392
Co-NC@Mo_2C	GCE	347	61	*Nano Energy* 2019, 57, 746
E-CoO_x	carbon fiber	249	50	*Nano Energy* 2019, 58, 778
Fe_1Co_3/V_O-800	GCE	260	53	*J. Mater. Chem. A* 2019, 7, 3090

Table S4. Atomic ratio of bi- and trimetallic MOFs extracted from XPS spectra.

Sample	Mn (atom.%)	Fe (atom.%)	Co (atom.%)	Ni (atom.%)	Cu (atom.%)
NiMn-MOF	47.6	------	------	52.4	------
NiFe-MOF	------	49.0	------	51.0	------
NiCo-MOF	------	------	51.4	48.6	------
NiCu-MOF	------	------	------	46.9	53.1
NiCoMn-MOF	31.5	------	34.3	34.2	------
NiCoFe-MOF	------	31.8	35.6	32.6	------
NiCoCu-MOF	------	------	33.9	33.6	32.5

References

1. T. Ma, F. Zhou, T. W. Zhang, H. B. Yao, T. Y. Su, Z. L. Yu, Y. Li, L. L. Lu and S. H. Yu, *Angew. Chem. Int. Ed.*, 2017, **56**, 11836-11840.
2. H. Hu, X. Lou, C. Li, X. Hu, T. Li, Q. Chen, M. Shen and B. Hu, *New J. Chem.*, 2016, **40**, 9746-9752.
3. S. Maiti, A. Pramanik, U. Manju and S. Mahanty, *ACS Appl. Mater. Interfaces*, 2015, **7**, 16357-16363.
4. F. L. Li, P. Wang, X. Huang, D. J. Young, H. F. Wang, P. Braunstein and J. P. Lang, *Angew. Chem. Int. Ed.*, 2019, **58**, 7051-7056.
5. Q. Liu, L. Yu, Y. Wang, Y. Ji, J. Horvat, M. L. Cheng, X. Jia and G. Wang, *Inorg. Chem.*, 2013, **52**, 2817-2822.
6. K. S. W. Sing, D. H. Everett, R. A. W. Haul, L. Moscou, R. A. Pierotti, J. Rouquerol and T. Siemieniewska, *Handbook of Heterogeneous Catalysis (eds G. Ertl, H. Knözinger, F. Schüth and J. Weitkamp)*, 2008, DOI: 10.1002/9783527610044.hetcat0065.
7. Y. Peng, Y. Li, Y. Ban, H. Jin, W. Jiao, X. Liu and W. Yang, *Science*, 2014, **346**, 1356.
8. D. B. Miracle and O. N. Senkov, *Acta Mater.*, 2017, **122**, 448-511.
9. M. A. Peck and M. A. Langell, *Chem. Mater.*, 2012, **24**, 4483-4490.
10. K. Rui, G. Zhao, Y. Chen, Y. Lin, Q. Zhou, J. Chen, J. Zhu, W. Sun, W. Huang and S. X. Dou, *Adv. Funct. Mater.*, 2018, **28**, 1801554.
11. Q. Qian, Y. Li, Y. Liu, L. Yu and G. Zhang, *Adv. Mater.*, 2019, **31**, 1901139.